WILEY | Hindawi

Research Article

Experimental Studies on Shale Cracks and Permeability Evolution Based on Acoustic Emission Monitoring

Hao Chen [ID],[1,2] **Hongkui Ge** [ID],[1,2] **Xiaoqiong Wang** [ID],[1,2] **Jianbo Wang** [ID],[3] **and Shan Wu** [ID][4]

[1]*Unconventional Oil and Natural Gas Institute, China University of Petroleum, Beijing 102249, China*
[2]*State Key Laboratory of Petroleum Resources and Prospecting, China University of Petroleum, Beijing 102249, China*
[3]*China University of Petroleum, Beijing at Karamay, Karamay 834000, China*
[4]*Department of Earth and Space Sciences, Southern University of Science and Technology, Shenzhen 518055, China*

Correspondence should be addressed to Hongkui Ge; gehongkui@163.com

The matrix permeability of shale reservoirs is extremely low. Therefore, massive volume fracturing is needed to form a complex crack network and get adequate sufficient capacity during the well completion. After fracturing, the effective stimulated reservoir volume (ESRV) is vital for developing shale reservoirs, mainly determined by stimulated reservoir volume (SRV) and the increase in permeability. Microseismic monitoring is widely used in the field to describe the crack shape and determine the SRV, to evaluate the stimulation effect. However, no studies have been conducted on the relationship between microseismic parameters and permeability. Thereby, we conducted uniaxial compression tests on Longmaxi shale samples and measured their changes in porosity and permeability before and after loading combining the microseismic monitoring under a laboratory scale (acoustic emission (AE)). Results show that porosity has little influence on the permeability before and after loading, while the propagation and connection of cracks are the most critical factors. As the loading stress increases, the crack volume and sample connectivity both grow. Besides, for the Longmaxi shale, when the stress is loaded to 30~50% of uniaxial compressive strength (UCS), the cracks start to propagate steadily (dilation), the permeability begins to increase rapidly, and percolation occurs, which indicates that the dilation point is closely related to the percolation threshold. The AE rate and accumulative ringing number both increase when it is larger than the percolation threshold value. The variation of AE characteristics can be used to identify the percolation threshold. Finally, the graphic model including AE parameters, crack, and permeability evolution is established based on the experimental results, which could help us understand the relationship between microseismic parameters and permeability and provide a methodological basis for the ESRV evaluation in the field.

1. Introduction

As a typical unconventional gas resource, shale gas reservoirs have extremely low porosity and permeability [1–3]. Large-scale hydraulic fracturing is required during the development to form a complex crack network and achieve efficient exploitation of shale gas [4–6]. Microseismic monitoring based on seismological theory is an effective method to describe the hydraulic crack formation, which is applied in the field to evaluate the characteristics of the fracturing network and SRV size [7–9]. Regions with signals around the cracks are treated as SRV in microseismic monitoring, yet not all cracks within the SRV have percolation capacity [10]. Therefore,

ESRV would be overestimated. Numerous field data and studies have shown that SRV is not the only factor that affects the stimulation; crack density and conductivity are also critical [11–13]. Hydraulic fracturing requires a specific stimulated volume and crack density to form the effective connections between natural cracks and bedding, cracks, and micro-nanopores with oil and gas storage, to increase reservoir permeability and achieve the ESRV.

During hydraulic fracturing, microcracks are generated in the reservoir matrix in addition to artificial cracks. According to the percolation theory, when microcracks reach the critical size, the reservoir changes from impermeable to permeable, which is called percolation, and the critical value

is the percolation threshold [14, 15]. After that, the permeability increases rapidly. Hence, understanding the crack evolution, identifying the percolation threshold, and establishing the relationship between microseismic characteristics and percolation threshold are essential to the fracturing evaluation.

Previous studies have been conducted on the crack geometry and density based on seismic data [12, 16, 17], but the relationship between microseismic crack and permeability has not been established due to the untestable permeability in the field. AE monitoring is microseismic monitoring on the laboratory scale, which is widely used to study the failure process of rocks and hydraulic fracturing in the laboratory [18–23].

Extensive experiments have been conducted to study the AE characteristics, crack, and permeability propagation of shale. There are mainly three types of researches. The first type is to study the crack evolution and failure mechanism under different loading patterns based on AE. The brittle failure of shale occurs during loading progress [24], and the bedding planes of shale have a significant effect on its mechanical behavior [25]. Tensile cracks along with the bedding dominate the failure of shale with the axis parallel to the bedding. The shale with the axis vertical to the bedding fails with complex fracture as it is affected by both shear and tensile cracks [19, 26]. The AE activities may be the response of the microstructural changes caused by the closure and development of pores and cracks at elevated stress [27]. The crack initiation occurred at approximately 30% of the UCS [24]. For shale with fluid, the failure is dominated by shear crack by analyzing the b-value of AE [28, 29]. The second type is to study the permeability variation with stress. Shale permeability increases under uniaxial stress damage, and the permeability variation is similar to that of stress damage [30]. In true triaxial stress conditions, the permeability decreases with the increase in principal stress. Still, the permeability variations caused by changing each principal stress are different. The permeability exhibits obvious bedding dependence, and the maximum decrease in permeability with increasing stress occurs in the direction vertical to the bedding [31–33]. The third type involves AE characteristics, cracks, and permeability evolution. Zhu et al. studied the influence of natural cracks on permeability and mechanical properties by AE energy. The orientation of natural fractures is closely related to permeability, AE events, and volume-strain value [34]. Based on percolation theory and AE data, Sakhaee-Pour and Agrawal established the model to predict the permeability evolution. A connected fracture is formed when the number of AE events per unit volume is larger than the threshold value. And the permeability remains close to the matrix when the number of AE events per unit volume is smaller than the threshold value [35].

Although plenty of researches have been conducted on shale mechanics, crack propagation, permeability, and AE activities, there is still a lack of comprehensive study on all the above parameters. In this paper, a series of experiments were carried out on shale to study the mechanical properties, AE characteristics, porosity, and permeability. Based on experimental data, the relationship between crack propagation, permeability, AE characteristics, and stress is obtained and the percolation threshold is identified. Furthermore, the connectivity of cracks acquired from the AE location is discussed to reveal the evolution mechanism of permeability. These results can provide a theoretical basis for ESRV estimation, thereby guiding the effective development of unconventional reservoirs.

2. Experimental Method

2.1. Sample Preparation. In this study, samples were taken from the marine sedimentary shale outcrop of the Lower Silurian Longmaxi Formation in Chongqing, SW China, as shown in Figures 1(a) and 1(b). The Longmaxi shale is bedding developed and rich in clay minerals and organic matter [36, 37]; see Figure 1(d) for the sample's mineral composition. Samples were taken from the same rock to reduce variability and cored successively in adjacent positions with coring direction paralleling the bedding direction. According to the international standard for rock mechanics experiment [38], six cylindrical shale samples were prepared. Each cylindrical sample has a nominal length of 50 mm and a diameter of 25 mm, and the sample parallelism was less than ±0.02 mm to meet the loading requirements. See Table 1 for the basic properties of the samples.

2.2. Experimental Apparatus. The sample porosity and permeability were measured in the State Key Laboratory of Petroleum Resources and Prospecting in the China University of Petroleum (Beijing). A KXD-III helium porosimeter based on double Boyle's law was adopted to measure the porosity. It is an effective method for shale porosity measurement in recent years [39, 40]. Figure 2 shows the illustration of the porosimeter. The test procedure is shown as follows: Firstly, the sample and calibration block were put into the sample cell and then close all valves, and the calibration block is used to reduce the dead volume of the sample cell. Secondly, open valve 1 to let gas enter the reference cell, close valve 1, when the pressure got stable, and record the pressure p_1, volume V_1, and temperature T_1. Finally, open valve 2 till the pressure is stable, and record p_2, V_2, and T_2. The calculation equation is given by

$$\frac{(p_1 + p_0)V_{rc} + p_0(V_{sc} - V_b - V_c + V_p)}{T_1} = \frac{(p_2 + p_0)(V_{rc} + V_{sc} - V_b - V_c + V_p)}{T_2}, \tag{1}$$

$$V_p = \frac{T_2((p_1 + p_0)V_{rc} + p_0(V_{sc} - V_b - V_c)) - T_1(p_2 + p_0)(V_{rc} + V_{sc} - V_b - V_c)}{T_1(p_2 + p_0) - T_2 p_0}, \tag{2}$$

where p_0 is the atmospheric pressure and A_{rc} and V_{sc} represent the reference cell and sample cell volume, respectively. V_c is the volume of the calibration block. V_b and V_p denote the bulk volume and porosity volume of the sample, respectively. The sample porosity (ϕ) is given by

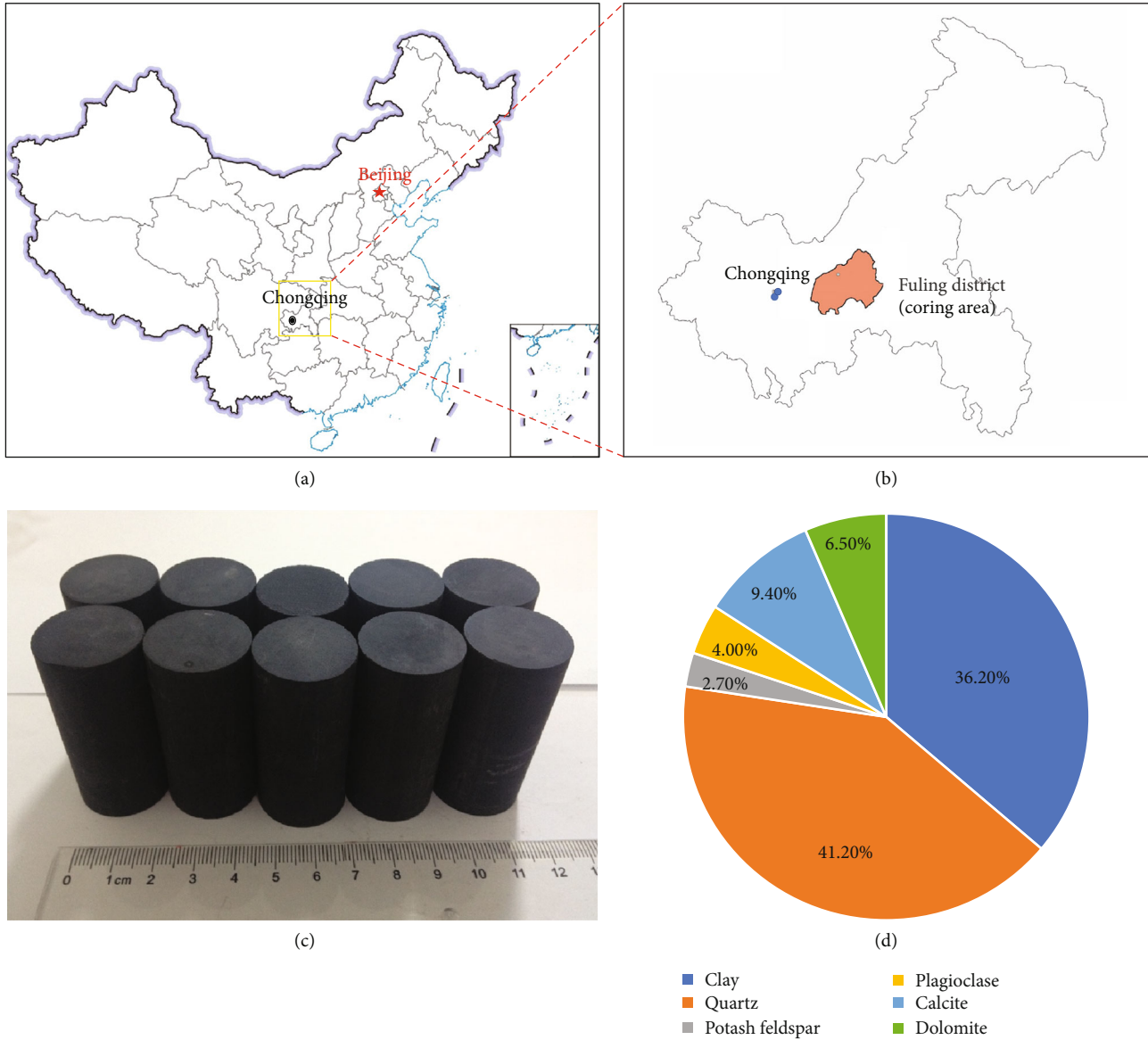$$\phi = \frac{V_p}{V_b} \times 100\%. \tag{3}$$

FIGURE 1: Experimental materials: (a) geographical location; (b) coring area; (c) samples; (d) mineral composition.

TABLE 1: Basic physical properties of the samples.

Sample	Length (mm)	Diameter (mm)	Mass (g)	Density (g/cm^3)	p-wave velocity (m/s)
Shale 1	50.30	24.28	59.20	2.54	3934
Shale 2	50.44	24.34	59.63	2.54	4042
Shale 3	51.20	24.25	59.93	2.53	4130
Shale 4	50.41	24.29	59.36	2.54	4066
Shale 5	50.34	24.22	58.92	2.54	4003
Shale 6	50.86	24.25	59.80	2.54	4058

As the shale permeability is extremely low, a YRD-CP200 pulse permeameter was adopted in this study. The pulse-decay method is a simple and accurate way to measure ultra-low permeability. Its testing principle is shown in Figure 3. The sample was jacketed into the core holder, and then, close all valves. Open valve 1, valve 2, and valve 3, and the sample is saturated with nitrogen; maintain the upstream pressure p_u and downstream pressure p_d consistent for a while. Then, open the microleakage valve, and decrease the downstream pressure with a small Δp to cause an instantaneous additional pressure difference between the upstream and downstream ends. As the fluid flows in the sample, the upstream pressure p_u decays exponentially till a new equilibrium pressure p_f is reached. The permeability k can be obtained through the measurement of the time it takes the fluid to flow through the sample and the exponential change in fluid pressure over time, which is given by

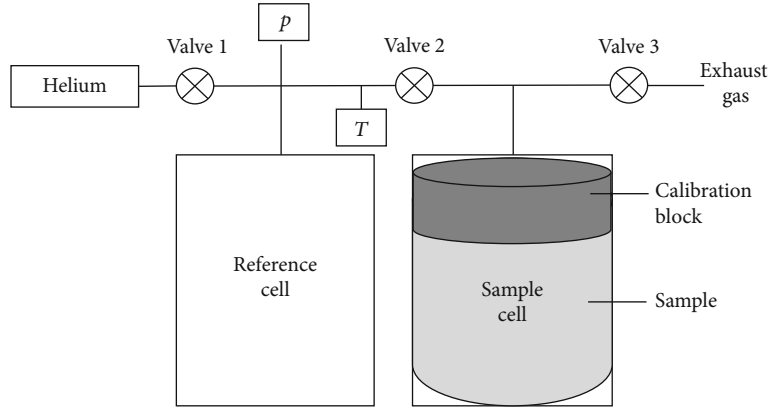$$k = \alpha \mu c_g \frac{L}{A} V_u. \tag{4}$$
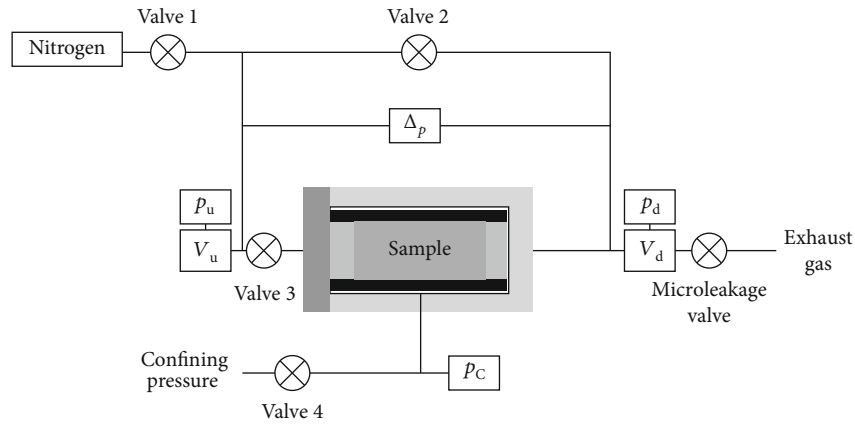
Figure 2: Schematic diagram of the porosimeter.

Figure 3: Schematic diagram of the pulse permeameter.

The attenuation index α can be obtained from the exponential attenuation of the fluid pressure:

$$p_u - p_f = \Delta p \frac{V_u}{V_u + V_d} e^{-\alpha t}, \tag{5}$$

where V_u and V_d denote the upstream and downstream container volume and α is the attenuation index. μ is the nitrogen viscosity. c_g is the compressibility of nitrogen. L and A are the length and cross-sectional area of the sample, respectively. During the test, the system automatically records data once for every 0.002 MPa attenuation of upstream pressure, and the final permeability is obtained by linear regression.

Samples were dried at 65°C for 24 hours before the porosity and permeability testing. The porosity was measured without confining pressure and under a pore pressure of 0.8 MPa and test temperature of 20°C. The permeability was measured under a confining pressure of 10 MPa and pore pressure of 6 MPa, and the test temperature was 20°C.

The mechanics and AE tests were conducted in the Institute of Geophysics, China Earthquake Administration, with the MTS-1000 kN loading system and PCI-2 acoustic emission system, as shown in Figure 4. The maximum loading of the MTS system is 1000 kN. The PCI-2 AE system from American Physical Acoustics Company (PAC) can collect 20 characteristic parameters such as AE event, AE energy, and ringing. The sampling rate is up to 40 MHz. Also, there are eight external parameters, which can introduce the MTS stress value and the strain value of the strain gauge into the AE acquisition system to keep the records time-synchronized. The two systems work simultaneously which could achieve the synchronous test of AE and mechanical parameters.

Nanotransducers with the size of Φ8mm × 8 mm and bandwidth of 50~750 kHz were used in this study. Six nanotransducers coated with coupling agents were placed symmetrically on the cylindrical sample to record the AE event's parameters and waveform and locate their position in real time. See Figure 5 for the transducer arrangement. Stress-controlled uniaxial loading was used in this experiment. Samples were tested under a 2 MPa/min rate of stress loading. And the AE sampling rate was 5 MHz, while the threshold value was 45 dB.

2.3. Experimental Methodology. AE location, mechanical properties, and permeability of the rock are tested in this study. Due to the limitation of sample size, the strain gauges and transducers cannot be arranged in the same sample.
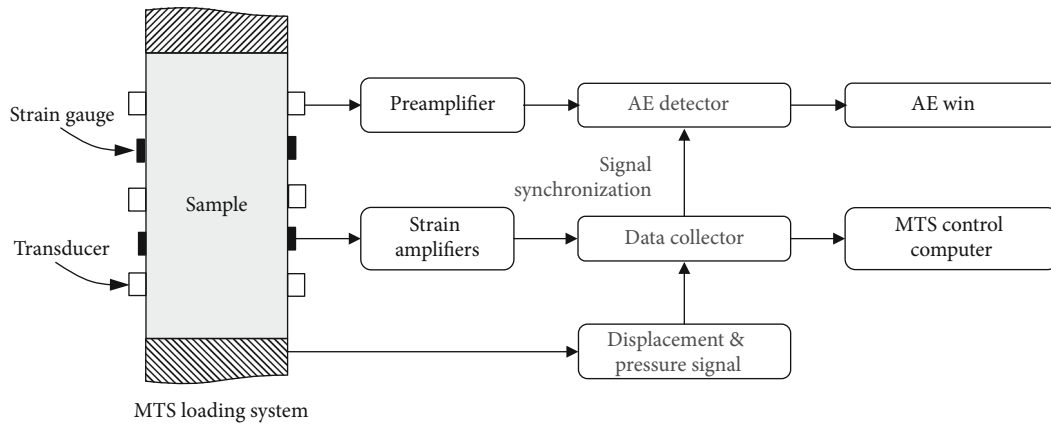
(a)
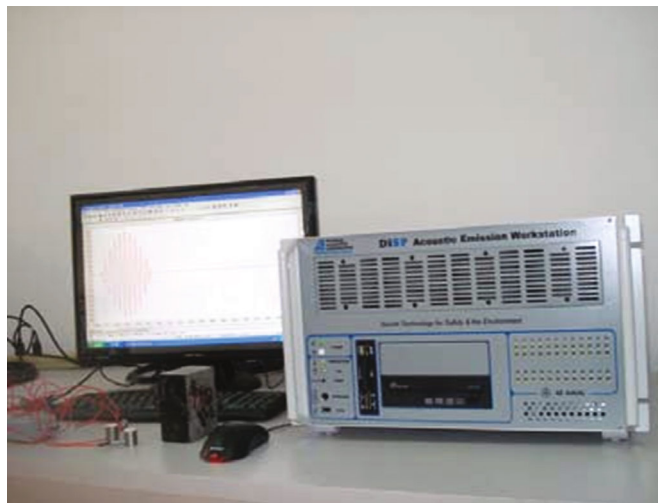
(b)

(c)

Figure 4: Schematic diagram of the test system of AE mechanics: (a) schematic diagram of the MTS-PCI-2 system; (b) PCI-2 AE system; (c) MTS loading system.

Meanwhile, the existing equipment cannot conduct AE location and permeability testing simultaneously. Therefore, the parallel experiment method is used in this research.

The test procedure consists of the following steps: (1) The samples were dried at 65°C for 24 h, and then, the basic parameters such as size, porosity, and permeability were
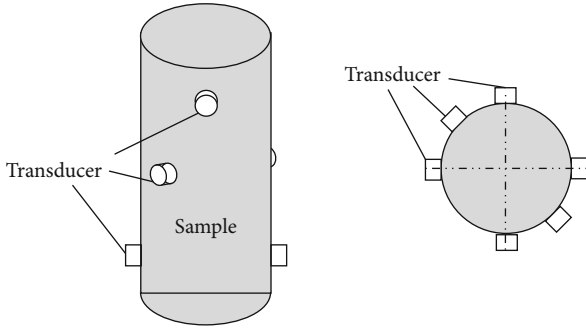
FIGURE 5: Illustration of the transducer arrangement.

measured. (2) Shale 6 was loaded under uniaxial stress until rupture, and then, the uniaxial compressive strength (UCS) of shale 6 was obtained. (3) To ensure the samples' integrity, shales 1-5 were loaded under uniaxial stress to about 15%, 35%, 50%, 70%, and 85% of the UCS of shale 6. Stop loading before the samples break, and record the stress and AE signals during the loading. (4) The porosity and permeability of shales 1-5 were measured. See Table 2 for the sample parameters that got tested.

3. Results

3.1. Shale Mechanical Properties. The stress-strain curve of shale 6 is shown in Figure 6, which is a typical brittle failure, and the maximum axial strain is about 0.4%. Many researchers have conducted comprehensive studies on the stress-strain curve [41–44]. According to the rock brittle failure theory proposed by Brace and Bieniawski, the stress-strain curve under uniaxial loading can be divided into five stages. In stage I, the curve is convex downward due to the closure of initial cracks. The microcracks are gradually compacted, and the strain change gradually slows down as the stress increases till it reaches the crack closing stress σ_{cc}. This stage could reflect the development of preexisting cracks. In stage II, the curve is a straight line with a stable slope, reflecting the rock's linear elastic deformation. Young's modulus and Poisson's ratio are both obtained in this stage. Stage III begins when the stress reaches the crack initiation stress σ_{ci}, and the slope starts to go down while the curve is convex upward. In this stage, cracks propagate stably, and new cracks are generated. The radial strain-stress and volumetric strain-stress curves become nonlinear. Rock dilation happens in this stage, and σ_{ci} is the dilation stress. Stage IV is the accelerated growth stage of cracks. As the stress reaches crack damage stress σ_{cd}, the volumetric strain is no longer reduced by compression but starts to expand, and the crack density increases significantly inside the rock. The last stage (stage V) is the postrupture stage. Shale strength drops instantly as the failure stress σ_f (UCS) is reached.

For shale 6, there are no prominent stable propagation stage and accelerated growth stage, and basically, no residual strength exists in the postpeak stage. And it is a typical brittle failure. From the stress-strain curve, the elastic modulus is 32.87 GPa, Poisson's ratio is 0.17, and the UCS is 122.69 MPa.

3.2. AE Characteristics. AE is a kind of transient elastic wave generated by the rapid release of an internal energy source inside the material [45]. AE accompanies crack propagation during the loading progress. A certain voltage is set artificially as a specific threshold voltage. The wave that exceeds the threshold voltage will form a rectangular impulse and is considered a ringing count [46]. The ringing counts could reflect the total amount and frequency of AE activities. The ringing counts per unit pressure are defined as the AE rate. For shales 1-5, the variation law of accumulative ringing counts and AE rate with stress is shown in Figures 7(a)– 7(e). For shale 1 and shale 2, the loading stress is relatively low, only a few AE signals are generated, AE activity is weak, and AE rate is low, while the accumulative ringing counts are small. The AE characteristics of shale 3, shale 4, and shale 5 during initial loading are consistent with those of shale 1 and shale 2. When the loading stress is between 45 and 60 MPa, AE activity begins to increase and AE rate and accumulative ringing counts increase significantly. Statistics show that the accumulated ringing counts of five samples increase as the maximum loading stress rises exponentially when the loading stress exceeds 60 MPa (see Figure 7(f)). Besides, the accumulative AE number of some samples would leap during the loading process, which indicates the generation of relatively large cracks inside the rocks [45].

A local change of material identified by several probes is considered an AE event. The spatial distribution of AE events can reflect the crack propagation inside the samples. The double-difference algorithm can effectively reduce the AE location error [47, 48] and can process the experimental data and obtain the AE event location. The AE event cannot reflect all cracks' position but can reflect the general area [49]. The location results shown in Figure 8 indicate that the AE event number increases as the loading stress increases. For shale 1 and shale 2, the AE event number is relatively small due to the lower loading stress and increased significantly as for shale 3 to shale 5. The ringing counts are much higher for shale 5, yet due to the bad connection of some transducers, the sensitivity decreases, which leads to bad AE location results and less locatable events. The AE location results of five samples are entirely discrete, which indicates that the cracks generated inside the rocks are random before shale rupture.

3.3. Permeability and Porosity before and after Loading. The sample porosity and permeability before and after loading are shown in Table 3. Results indicate that the permeability increases after loading, while the porosity changes very little. The permeability and porosity data are correlated, showing that the correlation is not good (see Figure 9).

The sample porosity and permeability data after loading are divided by the initial porosity and permeability data to obtain the dimensionless permeability k_D and porosity ϕ_D. The dimensionless permeability of the five samples increases as the maximum loading stress increases. While the maximum loading stress is low, the dimensionless permeability

TABLE 2: Details of the sample parameters that got tested.

| Sample no. | Maximum loading stress (MPa) | Sample parameters | | | | |
		Initial porosity and permeability	Porosity and permeability after loading	AE	Stress	Strain
Shale 1	20.96	√	√	√	√	×
Shale 2	42.43	√	√	√	√	×
Shale 3	61.40	√	√	√	√	×
Shale 4	86.77	√	√	√	√	×
Shale 5	100.00	√	√	√	√	×
Shale 6	122.69 (fractured)	√	×	×	√	√

Note: √ represents that the parameter was tested and × represents that the parameter was not tested.
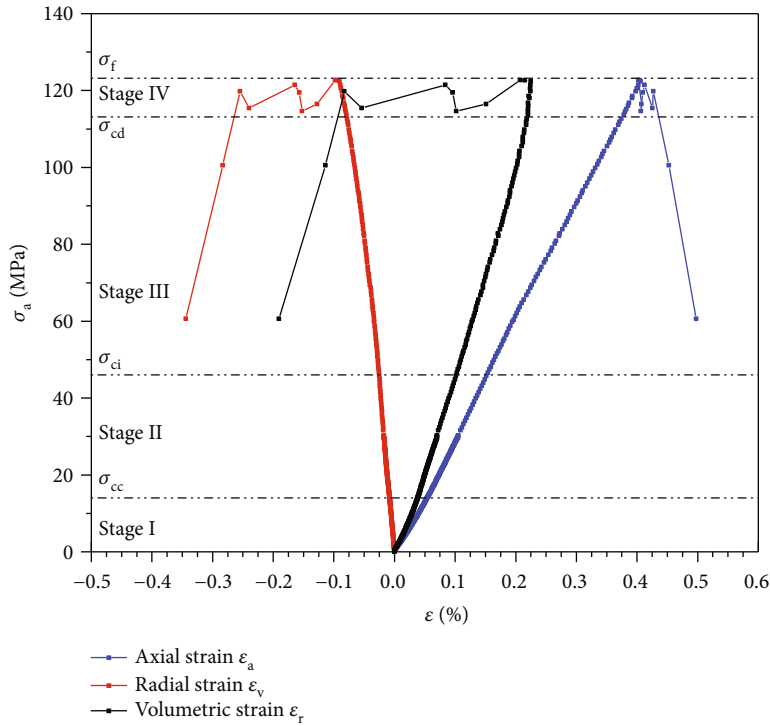

FIGURE 6: The stress-strain curve of shale 6. σ_a is the axial stress. ε is the strain. σ_{cc} is the crack closure stress. σ_{ci} is the crack initiation stress. σ_{cd} is the crack damage stress. σ_f is the failure stress. Stage I: initial crack closure. Stage II: linear elastic region. Stage III: stable crack propagation. Stage IV: unstable crack propagation.

changes very little. While the maximum loading stress is larger than 40 MPa, the dimensionless permeability increases exponentially and rapidly (see Figure 10). The percolation threshold of the samples appears between 40 and 60 MPa. The porosity of all the samples remains unchanged before and after the testing, indicating that the variation of the whole porosity contributes little to the increase in shale permeability before fracturing.

4. Discussions

4.1. Percolation Behavior of Shale during Uniaxial Loading. The ratio of the minimum to the maximum diameter of rock pores is called the aspect ratio, according to which pores can be divided into nearly spherical holes and narrow-long cracks. The effect of cracks on rock porosity is small, but it can significantly affect the permeability [50, 51]. Based on the percolation theory, continuous flow channels initially exist in the rock, yet there are not enough connected cracks to form a network. Therefore, rock permeability is extremely low. As the loading progresses, the crack number increases gradually. The size of the connected group inside the formation shows nonlinear growth. A noticeable permeability jump occurs at the percolation threshold, while the formation permeability increases rapidly.
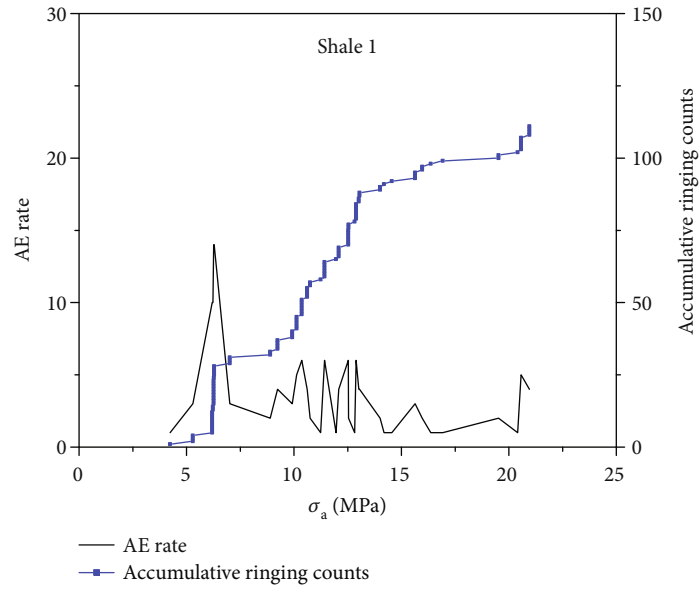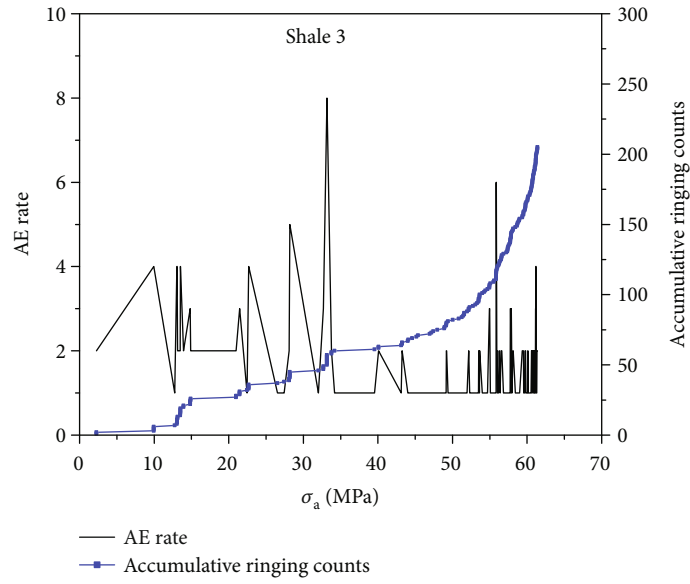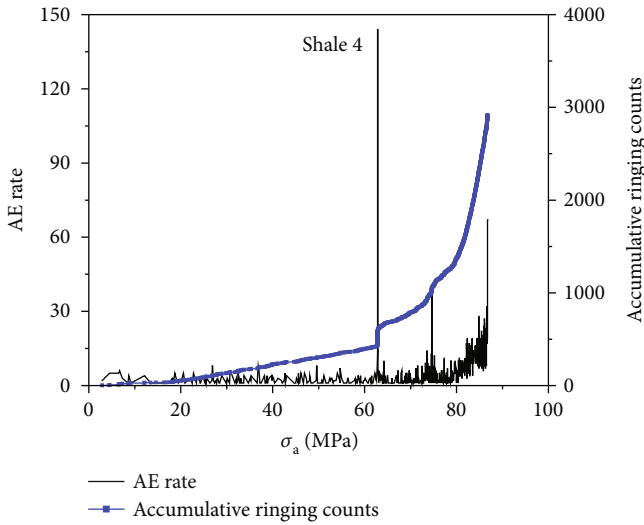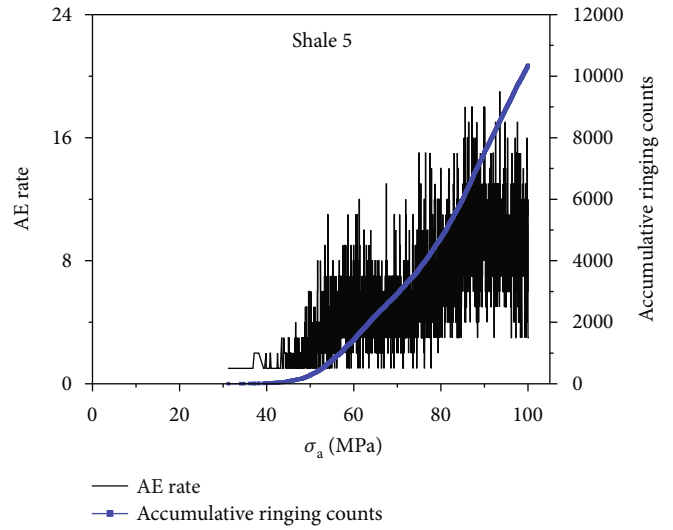
(a)
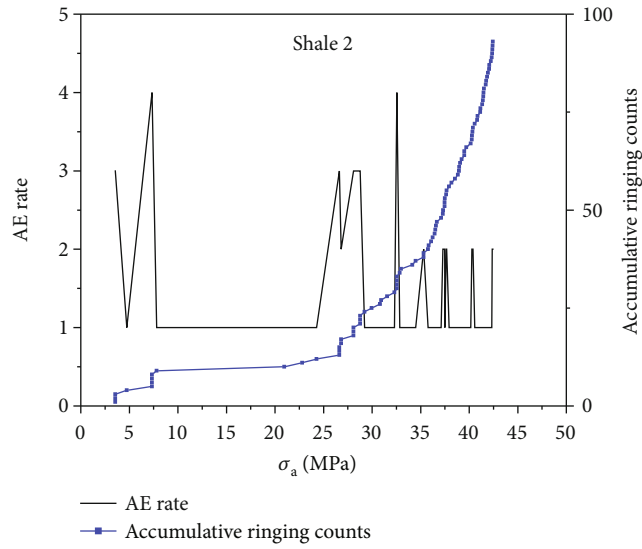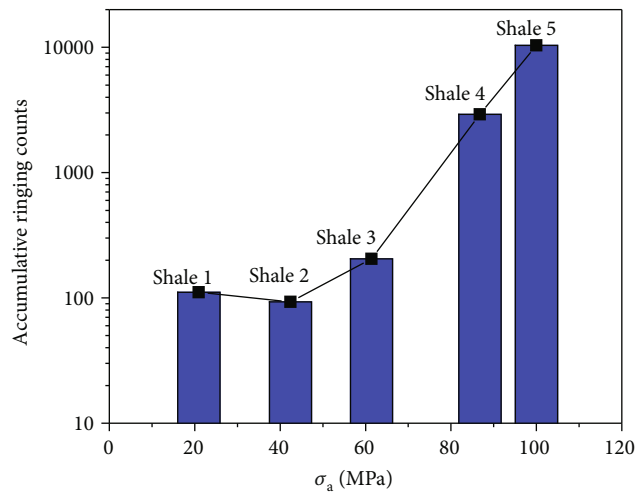

(b)

Figure 7: Continued.

(c)

(d)

(e)

(f)

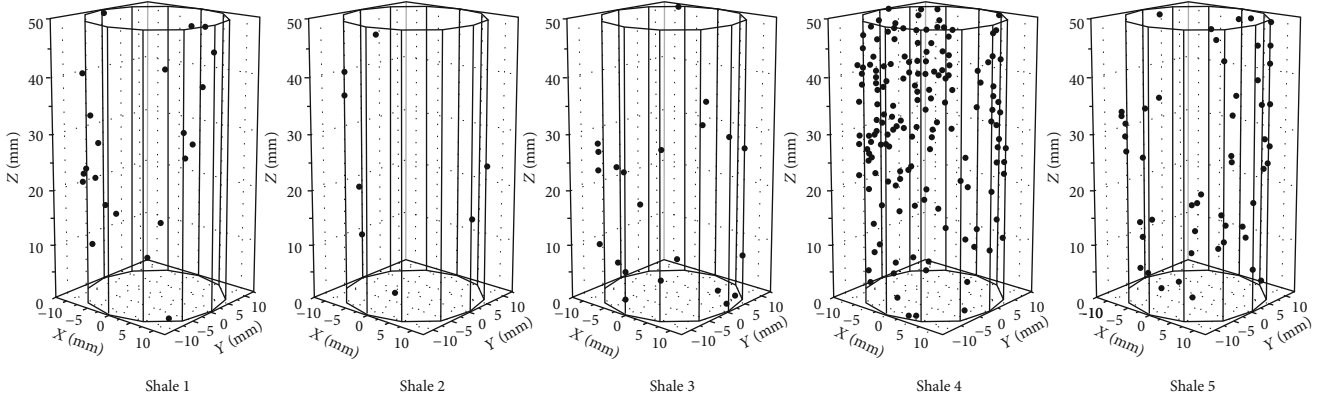FIGURE 7: AE rate and accumulative ringing counts under loading stress.

FIGURE 8: AE location results of the samples.

TABLE 3: The permeability and porosity before and after loading.

Sample	Before loading		After loading	
	Porosity ϕ (%)	Permeability k (m^2)	Porosity ϕ (%)	Permeability k (m^2)
Shale 1	3.56	2.12×10^{-19}	3.71	2.22×10^{-19}
Shale 2	3.74	2.28×10^{-19}	3.70	2.50×10^{-19}
Shale 3	4.02	1.67×10^{-18}	4.11	2.73×10^{-18}
Shale 4	3.34	1.25×10^{-19}	3.38	2.94×10^{-19}
Shale 5	2.95	1.82×10^{-19}	2.99	8.25×10^{-19}
Shale 6	3.64	1.12×10^{-19}		

The evolution laws of shale mechanics, AE characteristics, porosity, and permeability under uniaxial stress can be observed from Figures 6–10. As the axial stress is loaded to 40~60 MPa, the shale permeability increases significantly to the percolation threshold, and percolation occurs. The AE ringing counts and AE rate are very low before the percolation threshold is reached; the stress-strain curve is in the linear elastic stage. In contrast, the AE ringing counts and AE rate increase significantly after the percolation threshold is reached, and the stress-strain curve is nonlinear. The percolation threshold corresponds to the dilation point, and the porosity changes very little before and after loading. In this paper, assume that the mechanics of shale 6 represent the mechanics of all the samples. The Longmaxi shale's percolation threshold is 30-50% of UCS, which corresponds to the initial dilation stress σ_{ci}.

4.2. Percolation Mechanism: Generation and Connection of Cracks. Based on the rock brittle failure theory, Martin and Chandler proposed a method to calculate the crack volume deformation [43]. The volumetric strain of the rock ε_v is obtained by

$$\varepsilon_v = \frac{\Delta V}{V} = \varepsilon_a + 2\varepsilon_r, \tag{6}$$

where ΔV is the volume deformation of the rock. V is the

rock volume. ε_a and ε_r are the axial and radial strain, respectively. According to the elastic modulus E and Poisson's ratio v calculated from the linear elastic stage in the rock stress-strain curve, the elastic volumetric strain of the rock ε_{ve} can be written by

$$\varepsilon_{ve} = \frac{1 - 2v}{E}\sigma_a. \tag{7}$$

The crack volumetric strain ε_{vc} can be described as

$$\varepsilon_{vc} = \varepsilon_v - \varepsilon_{ve}. \tag{8}$$

We can see the crack evolution during the loading process from the crack volumetric strain-axial strain curve, as shown in Figure 11. σ_{cc} and σ_{ci} are the stresses corresponding to the initial and end position of the parallel section in the curve, respectively. Cracks could close quickly under very small loading stress before σ_{cc}. Between σ_{cc} and σ_{ci}, the crack volume remains the same. And massive cracks are generated while the loading stress is larger than σ_{ci}. The dimensionless permeability is negatively correlated with the crack volumetric strain, as shown in Figure 12. From the figure, σ_{cc} is 14 MPa while σ_{ci} is 46 MPa, and the percolation threshold is also around σ_{ci}. When the axial strain is 14 MPa, the initial crack porosity obtained is 0.010%. The maximum crack porosity near rupture is 0.049%. Both are far less than the porosity before and after loading which is 3.64%. The crack volume accounts for less than 2% of the total pore volume.

Succolarity is one of the essential parameters in fractal geometry theory. For porous medium, succolarity represents the fluid flow capacity inside the medium, which can be used to characterize the connectivity of the porous medium in different directions [52]. In this paper, we created a cube grid in three-dimensional coordinates, and each AE event represents a crack. The grids with cracks are connected, while the grids without cracks are not. By applying virtual fluid pressure in different directions, the succolarity values in six directions are obtained by calculating the proportion of the grid number with fluid flow to the total grid number using the gliding box counting method. A detailed description of the 3D succolarity calculation method can be found in Xia et al. [53].
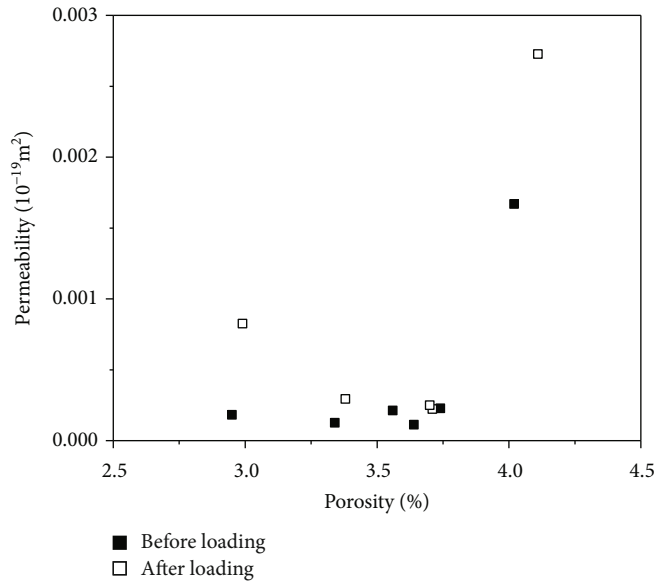
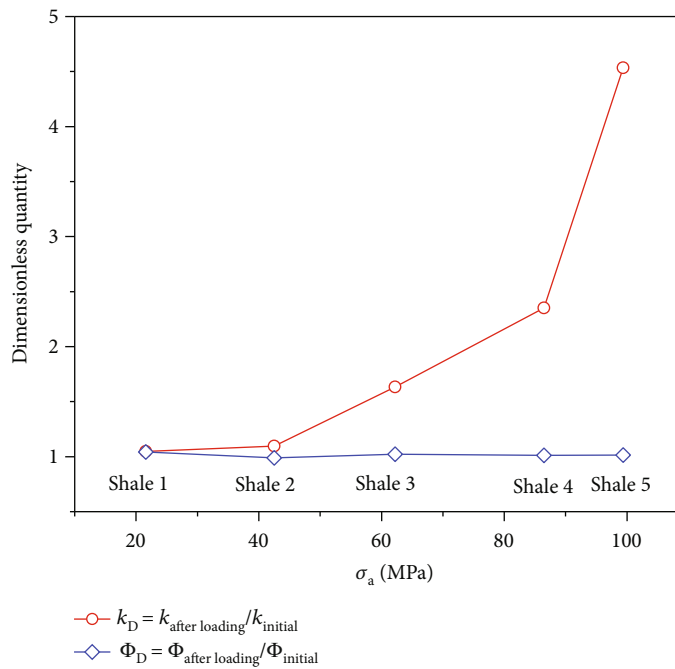FIGURE 9: Relationship between permeability and porosity.

FIGURE 10: The dimensionless permeability and porosity under stress.

In this paper, coordinates established during the succolarity calculation are consistent with the AE location coordinates.

The succolarity values of shales 1-4 in six directions are shown in Figure 13(a). Due to the sample differences, the correlation between succolarity and maximum loading stress is not good but shows an overall upward trend, and the succolarity value increases significantly from shale 3 to shale 4. In order to eliminate the influence of sample differences, shale 4 was analyzed separately. The accumulative AE events of shale 4 and their locations under

different stresses (20, 40, 60, and 86 MPa) were analyzed separately, as shown in Figure 14. Figure 13(b) shows the succolarity-stress curves of shale 4. The succolarity values in $Y+$ and $Z-$ directions remain zero, which indicates that there are no cracks in the two directions or the cracks generated are disconnected. Succolarity improves in the other four directions as the stress increases and shows a good correlation. The succolarity improves remarkably when the stress is between 40 and 60 MPa, which means that the crack connectivity is significantly enhanced in this
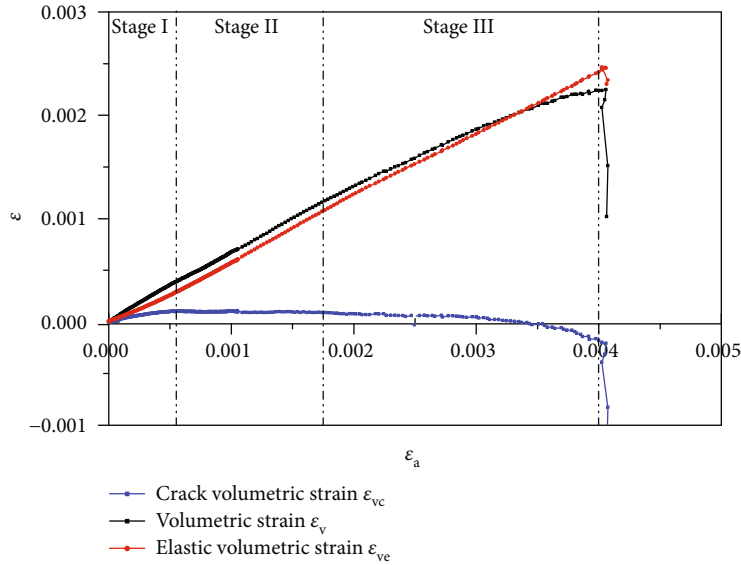
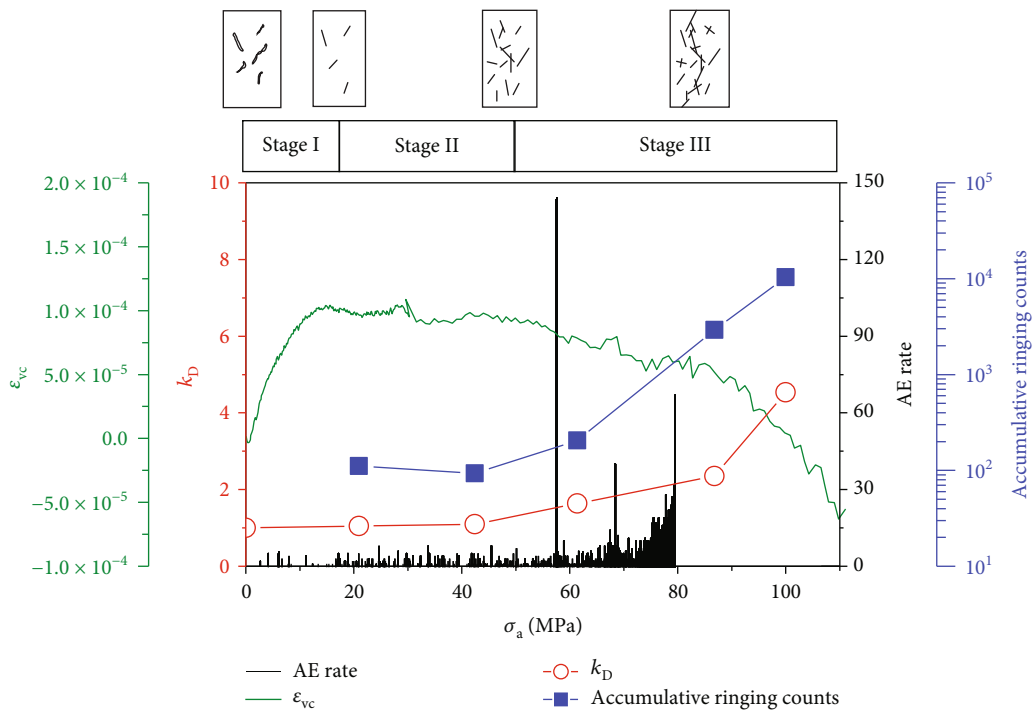FIGURE 11: Calculated crack volumetric strain.

FIGURE 12: The model diagram of AE characteristics, crack propagation, and permeability evolution.

stress interval. It is consistent with the interval where σ_{ci} and percolation threshold occur.

The calculation of crack volumetric strain could reflect the crack generation process under stress, while the crack connectivity can be obtained through the statistics of sample succolarity. Combining both, we can obtain the generation and connection of cracks during the loading, which is also the main mechanism affecting the percolation threshold.

Figure 12 shows the change of mechanics, AE characteristics (accumulative ringing counts and AE rate), porosity, and permeability of shale under uniaxial loading. According to the loading stress, the curve can be divided into three stages. In stage I and stage II, the initial cracks are closed, the AE ringing counts and AE rate are low, and the porosity and permeability remain unchanged. As the stress loaded reaches σ_{ci}, the
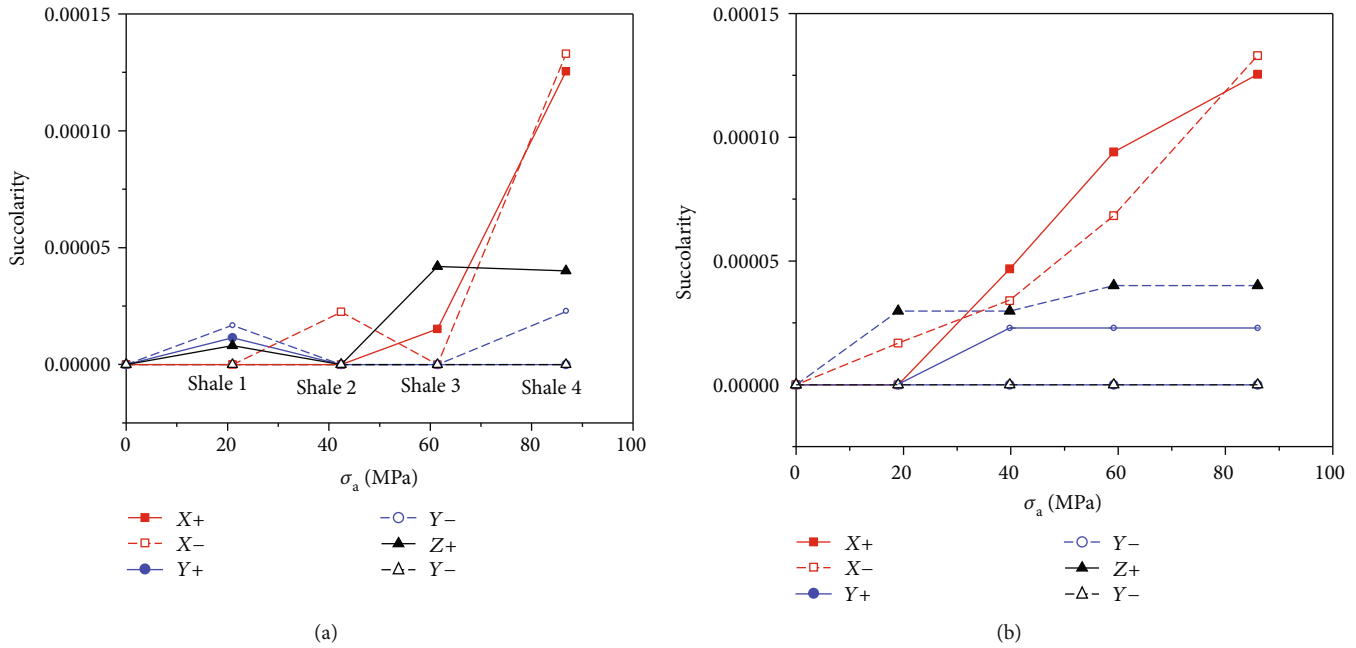
(a)

(b)

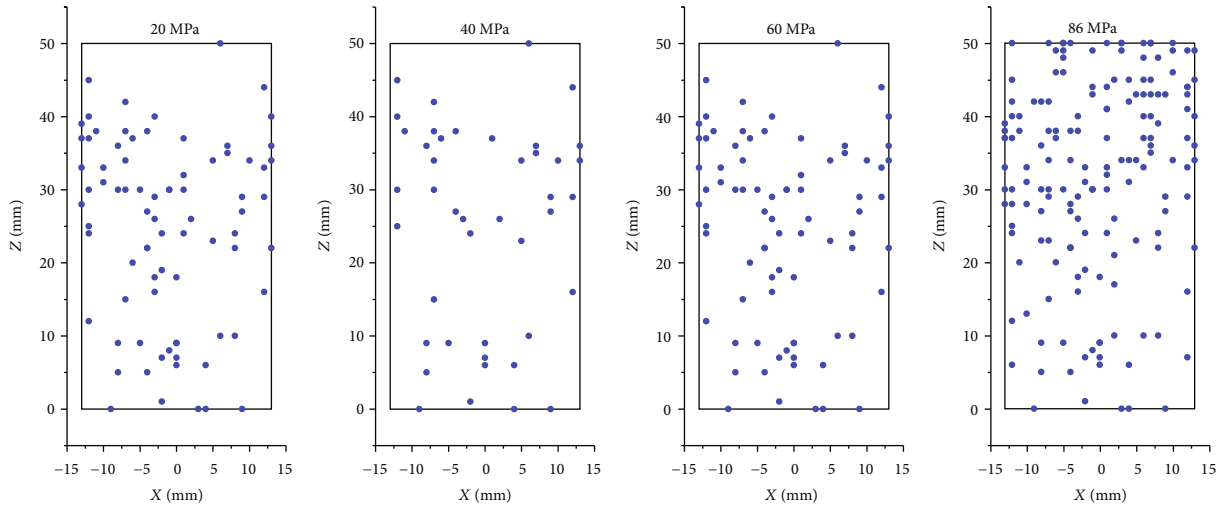FIGURE 13: The succolarity-stress curve: (a) shales 1-4; (b) shale 4 under different stresses.

FIGURE 14: The projections of AE locations under different stresses of shale 4.

generation of new cracks leads to a significant increase in the AE rate and permeability.

Based on the above analysis, we established a graphic model of cracks, permeability, and AE characteristics and then discussed the generation mechanisms of the percolation threshold. The study could help understand the relationship between AE characteristics, crack propagation, and permeability, thus improving the microseismic monitoring accuracy of hydraulic fracturing.

5. Conclusions

In this paper, we studied the AE characteristics (AE rate, accumulative ringing counts, and AE localization), crack vol-

ume based on stress-strain calculation, crack connectivity obtained from succolarity, and permeability evolution. The main conclusions are obtained as follows:

(1) The sample porosity is unchanged before and after 5loading, while the permeability changes significantly, and the porosity has little effect on permeability during the loading. Although cracks account for less than 2% of the pore volume, their generation and connection are the main control mechanisms of permeability evolution, which can be characterized by the crack volume calculated from stress-strain and succolarity gained by AE location, respectively

(2) The cracks begin to propagate stably at the dilation point (30-50% of UCS). Meanwhile, the succolarity and crack volume start to increase rapidly, and the permeability threshold appears. The sample dilatancy is the main micromechanism of the percolation threshold

(3) The AE rate and accumulative ringing counts are relatively low when the loading stress is smaller than the stress at the percolation threshold but increases significantly while the stress is larger than that. Therefore, AE characteristics can be used to identify the range of percolation threshold roughly

Data Availability

The data used to support the findings of this study are available from the corresponding author upon request.

Conflicts of Interest

The authors declare that there is no conflict of interest regarding the publication of this paper.

Acknowledgments

References

[1] C. H. Sondergeld, R. J. Ambrose, C. S. Rai, and J. Moncrieff, "Micro-structural studies of gas shales," in *SPE Unconventional Gas Conference*, Society of Petroleum Engineers, 2010.

[2] H. H. Liu, P. G. Ranjith, D. T. Georgi, and B. T. Lai, "Some key technical issues in modelling of gas transport process in shales: a review," *Geomechanics and Geophysics for Geo-Energy and Geo-Resources*, vol. 2, no. 4, pp. 231–243, 2016.

[3] R. Sander, Z. Pan, and L. D. Connell, "Laboratory measurement of low permeability unconventional gas reservoir rocks: a review of experimental methods," *Journal of Natural Gas Science and Engineering*, vol. 37, pp. 248–279, 2017.

[4] T. Guo, S. Zhang, Z. Qu, T. Zhou, Y. Xiao, and J. Gao, "Experimental study of hydraulic fracturing for shale by stimulated reservoir volume," *Fuel*, vol. 128, pp. 373–380, 2014.

[5] C. Zou, D. Dong, S. Wang et al., "Geological characteristics and resource potential of shale gas in China," *Petroleum Exploration and Development*, vol. 37, no. 6, pp. 641–653, 2010.

[6] B. Roychaudhuri, T. T. Tsotsis, and K. Jessen, "An experimental investigation of spontaneous imbibition in gas shales," *Journal of Petroleum Science and Engineering*, vol. 111, pp. 87–97, 2013.

[7] M. K. Fisher, C. A. Wright, B. M. Davidson et al., "Integrating fracture-mapping technologies to improve stimulations in the Barnett shale," *SPE Production and Facilities*, vol. 20, no. 2, pp. 85–93, 2005.

[8] S. C. Maxwell, T. I. Urbancic, C. Demerling, and M. Prince, "Real-time 4D passive seismic imaging of hydraulic fracturing," in *Proceedings of the SPE/ISRM Rock Mechanics in Petroleum Engineering Conference*, pp. 298–307, Irving, Texas, 2002.

[9] Z. Wei and Z. Siyu, "Application of surface microseismic monitoring technology in shale gas well fracturing of South Sichuan," *Reservoir Evaluation and Development*, vol. 4, pp. 71–74, 2014.

[10] M. Y. Cui, Y. Z. Liu, N. L. Xiu et al., "Analysis of factors affecting the formation of effective stimulated reservoir volume (ESRV)," *Oil Drilling & Production Technology*, vol. 36, pp. 82–87, 2014.

[11] M. J. Mayerhofer, E. P. Lolon, N. R. Warpinski, C. L. Cipolla, D. Walser, and C. M. Rightmire, "What is stimulated reservoir volume?," *SPE Production and Operations*, vol. 25, no. 1, pp. 89–98, 2010.

[12] S. C. Maxwell, C. Waltman, N. R. Warpinski, M. J. Mayerhofer, and N. Boroumand, "Imaging seismic deformation induced by hydraulic fracture complexity," *SPE Reservoir Evaluation and Engineering*, vol. 12, no. 1, pp. 48–52, 2009.

[13] Q. Zhang, Y. Su, W. Wang, and G. Sheng, "A new semi-analytical model for simulating the effectively stimulated volume of fractured wells in tight reservoirs," *Journal of Natural Gas Science and Engineering*, vol. 27, pp. 1834–1845, 2015.

[14] J. E. Ramírez, E. Molina-Gayosso, J. Lozada-Lechuga, L. M. Flores-Rojas, M. I. Martínez, and A. F. Téllez, "Percolation strategy to improve the production of plants with high pathogen susceptibility," *Physical Review E*, vol. 98, pp. 1–10, 2018.

[15] M. Colombier, F. B. Wadsworth, L. Gurioli et al., "The evolution of pore connectivity in volcanic rocks," *Earth and Planetary Science Letters*, vol. 462, pp. 99–109, 2017.

[16] M. J. Mayerhofer, E. P. Lolon, J. E. Youngblood, and J. R. Heinze, "Integration of microseismic fracture mapping results with numerical fracture network production modeling in the Barnett shale," in *SPE Annual Technical Conference and Exhibition*, vol. 2, pp. 976–983, San Antonio, Texas, USA, 2006.

[17] R. Meek, B. Suliman, H. Bello, and R. A. Hull, "Well space modeling, SRV prediction using microseismic, seismic rock properties and structural attributes in the Eagle Ford Shale of South Texas," in *Unconventional Resources Technology Conference (URTeC)*, pp. 1601–1608, San Antonio, Texas, USA, 2015.

[18] B. Liu, Y. Ma, G. Zhang, and W. Xu, "Acoustic emission investigation of hydraulic and mechanical characteristics of muddy sandstone experienced one freeze-thaw cycle," *Cold Regions Science and Technology*, vol. 151, pp. 335–344, 2018.

[19] Z. Moradian, A. Seiphoori, and B. Evans, "The role of bedding planes on fracture behavior and acoustic emission response of shale under unconfined compression," in *51st US Rock Mechanics / Geomechanics Symposium 2017 2017*, vol. 5, pp. 3328–3336, San Francisco, California, USA, 2017.

[20] N. Li, S. Zhang, Y. Zou et al., "Acoustic emission response of laboratory hydraulic fracturing in layered shale," *Rock Mechanics and Rock Engineering*, vol. 51, no. 11, pp. 3395–3406, 2018.

[21] H. Zhai, X. Chang, Y. Wang, X. Lei, and Z. Xue, "Analysis of acoustic emission events induced during stress unloading of a hydraulic fractured Longmaxi shale sample," *Journal of Petroleum Science and Engineering*, vol. 189, p. 106990, 2020.

[22] J. Tan, J. Xie, L. Li, Q. Lyu, J. Han, and Z. Zhao, "Multifractal analysis of acoustic emissions during hydraulic fracturing experiments under uniaxial loading conditions: a Niutitang shale example," *Geofluids*, vol. 2020, Article ID 8845292, 19 pages, 2020.

[23] Z. Moradian, H. H. Einstein, and G. Ballivy, "Detection of cracking levels in brittle rocks by parametric analysis of the acoustic emission signals," *Rock Mechanics and Rock Engineering*, vol. 49, no. 3, pp. 785–800, 2016.

[24] F. Amann, E. A. Button, K. F. Evans, V. S. Gischig, and M. Blümel, "Experimental study of the brittle behavior of clay shale in rapid unconfined compression," *Rock Mechanics and Rock Engineering*, vol. 44, no. 4, pp. 415–430, 2011.

[25] Y. Wang, C. H. Li, and Y. Z. Hu, "Experimental investigation on the fracture behaviour of black shale by acoustic emission monitoring and CT image analysis during uniaxial compression," *Geophysical Journal International*, vol. 213, no. 1, pp. 660–675, 2018.

[26] P. Hou, F. Gao, Y. Ju et al., "Experimental investigation on the failure and acoustic emission characteristics of shale, sandstone and coal under gas fracturing," *Journal of Natural Gas Science and Engineering*, vol. 35, pp. 211–223, 2016.

[27] X. Li, X. Lei, Q. Li, and X. Li, "Experimental investigation of Sinian shale rock under triaxial stress monitored by ultrasonic transmission and acoustic emission," *Journal of Natural Gas Science and Engineering*, vol. 43, pp. 110–123, 2017.

[28] D. Liu, Z. Wang, X. Zhang, Y. Wang, X. Zhang, and D. Li, "Experimental investigation on the mechanical and acoustic emission characteristics of shale softened by water absorption," *Journal of Natural Gas Science and Engineering*, vol. 50, pp. 301–308, 2018.

[29] F. Meng, H. Ge, W. Yan, X. Wang, S. Wu, and J. Wang, "Effect of saturated fluid on the failure mode of brittle gas shale," *Journal of Natural Gas Science and Engineering*, vol. 35, pp. 624–636, 2016.

[30] C. Yan, Y. Cheng, F. Deng, and J. Tian, "Permeability change caused by stress damage of gas shale," *Energies*, vol. 10, no. 9, p. 1350, 2017.

[31] M. Li, G. Yin, J. Xu, J. Cao, and Z. Song, "Permeability evolution of shale under anisotropic true triaxial stress conditions," *International Journal of Coal Geology*, vol. 165, pp. 142–148, 2016.

[32] C. Liu, G. Yin, M. Li et al., "Shale permeability model considering bedding effect under true triaxial stress conditions," *Journal of Natural Gas Science and Engineering*, vol. 68, p. 102908, 2019.

[33] Y. Chen, C. Jiang, G. Yin, D. Zhang, H. Xing, and A. Wei, "Permeability evolution under true triaxial stress conditions of Longmaxi shale in the Sichuan Basin, Southwest China," *Powder Technology*, vol. 354, pp. 601–614, 2019.

[34] H. Y. Zhu, L. Tao, Q. Y. Liu, Z. D. Lei, S. Jiang, and J. D. McLennan, "Fracture characteristics and change of permeability under the influence of natural fractures: experimental study of Wufeng-Longmaxi shale," *SPE Reservoir Evaluation & Engineering*, vol. 21, no. 2, pp. 225–237, 2018.

[35] A. Sakhaee-Pour and A. Agrawal, "Integrating acoustic emission into percolation theory to predict permeability enhancement," *Journal of Petroleum Science and Engineering*, vol. 160, pp. 152–159, 2018.

[36] K. Zhang, J. Peng, W. Liu et al., "The role of deep geofluids in the enrichment of sedimentary organic matter: a case study of the late Ordovician-Early Silurian in the upper Yangtze region and early Cambrian in the lower Yangtze region, south china," *Geofluids*, vol. 2020, Article ID 8868638, 12 pages, 2020.

[37] K. Zhang, J. Peng, X. Wang et al., "Effects of thermal evolution of organic matter on the genesis of shale gas and the development of organic matter pores: a case study of marine shale in the upper Yangtze region, South China," *Open Geosciences*, vol. 12, no. 1, pp. 1617–1629, 2020.

[38] R. Ulusay, *The ISRM Suggested Methods for Rock Characterization, Testing and Monitoring: 2007-2014*, Springer International Publishing, 2014.

[39] F. Yang, Z. Ning, Q. Wang, R. Zhang, and B. M. Krooss, "Pore structure characteristics of lower Silurian shales in the southern Sichuan Basin, China: insights to pore development and gas storage mechanism," *International Journal of Coal Geology*, vol. 156, pp. 12–24, 2016.

[40] L. Pan, X. Xiao, H. Tian et al., "A preliminary study on the characterization and controlling factors of porosity and pore structure of the Permian shales in lower Yangtze region, Eastern China," *International Journal of Coal Geology*, vol. 146, pp. 68–78, 2015.

[41] W. F. Brace, B. W. Paulding, and C. Scholz, "Dilatancy in the fracture of crystalline rocks," *Journal of Geophysical Research*, vol. 71, no. 16, pp. 3939–3953, 1966.

[42] Z. T. Bieniawski, "Mechanism of brittle fracture of rock: part III–fracture in tension and under long-term loading," *International Journal of Rock Mechanics and Mining Sciences & Geomechanics Abstracts*, vol. 4, no. 4, pp. 425–430, 1967.

[43] C. D. Martin and N. A. Chandler, "The progressive fracture of Lac du Bonnet granite," *International Journal of Rock Mechanics and Mining Sciences & Geomechanics Abstracts*, vol. 31, no. 6, pp. 643–659, 1994.

[44] F. Amann, Ö. Ündül, and P. K. Kaiser, "Crack initiation and crack propagation in heterogeneous sulfate-rich clay rocks," *Rock Mechanics and Rock Engineering*, vol. 47, no. 5, pp. 1849–1865, 2014.

[45] X. Wang, H. Ge, D. Wang, J. Wang, and H. Chen, "A comprehensive method for the fracability evaluation of shale combined with brittleness and stress sensitivity," *Journal of Geophysics and Engineering*, vol. 14, no. 6, pp. 1420–1429, 2017.

[46] F. Xiangqian, H. Shaowei, L. Jun, and W. Congjie, "Acoustic emission properties of concrete on dynamic tensile test," *Construction and Building Materials*, vol. 114, pp. 66–75, 2016.

[47] F. Waldhauser and W. L. Ellsworth, "A double-difference earthquake location algorithm: method and application to the Northern Hayward Fault, California," *Bulletin of the Seismological Society of America*, vol. 90, no. 6, pp. 1353–1368, 2000.

[48] S. Wu, T. Li, H. Ge, X. Wang, N. Li, and Y. Zou, "Shear-tensile fractures in hydraulic fracturing network of layered shale," *Journal of Petroleum Science and Engineering*, vol. 183, article 106428, 2019.

[49] J. P. Liu, Y. H. Li, and Y. J. Yang, "Study on characteristics of percolation in rock failure process via acoustic emission locating technique," *Dongbei Daxue Xuebao/Journal of Northeastern University*, vol. 31, pp. 1769–1772, 2010.

[50] P. M. Benson, P. G. Meredith, and A. Schubnel, "Role of void space geometry in permeability evolution in crustal rocks at elevated pressure," *Journal of Geophysical Research: Solid Earth*, vol. 111, no. B12, pp. 1–14, 2006.

[51] Y. Guéguen and A. Schubnel, "Elastic wave velocities and permeability of cracked rocks," *Tectonophysics*, vol. 370, no. 1-4, pp. 163–176, 2003.

[52] R. H. C. De Melo and A. Conci, "Succolarity: defining a method to calculate this fractal measure," in *Proceedings of IWSSIP 2008 - 15th International Conference on Systems Signals and Image Processing*, vol. 1, pp. 291–294, Bratislava, Slovakia, 2008.

[53] Y. Xia, J. Cai, E. Perfect, W. Wei, Q. Zhang, and Q. Meng, "Fractal dimension, lacunarity and succolarity analyses on CT images of reservoir rocks for permeability prediction," *Journal of Hydrology*, vol. 579, article 124198, 2019.